



## Unwinding Entangled Degradation Mechanisms in Solid Oxide Electrolysis Cells Through Electrode Modifications and Impedance Analysis

Rao, M.; Jensen, S. H.; Sun, X.; Hagen, A.

*Published in:*  
Fuel Cells

*Link to article, DOI:*  
[10.1002/face.201800166](https://doi.org/10.1002/face.201800166)

*Publication date:*  
2019

*Document Version*  
Publisher's PDF, also known as Version of record

[Link back to DTU Orbit](#)

*Citation (APA):*  
Rao, M., Jensen, S. H., Sun, X., & Hagen, A. (2019). Unwinding Entangled Degradation Mechanisms in Solid Oxide Electrolysis Cells Through Electrode Modifications and Impedance Analysis. *Fuel Cells*, 19(4), 445-457. <https://doi.org/10.1002/face.201800166>

---

### General rights

Copyright and moral rights for the publications made accessible in the public portal are retained by the authors and/or other copyright owners and it is a condition of accessing publications that users recognise and abide by the legal requirements associated with these rights.

- Users may download and print one copy of any publication from the public portal for the purpose of private study or research.
- You may not further distribute the material or use it for any profit-making activity or commercial gain
- You may freely distribute the URL identifying the publication in the public portal

If you believe that this document breaches copyright please contact us providing details, and we will remove access to the work immediately and investigate your claim.



# Unwinding Entangled Degradation Mechanisms in Solid Oxide Electrolysis Cells Through Electrode Modifications and Impedance Analysis<sup>▲</sup>

M. Rao<sup>1\*</sup>, S. H. Jensen<sup>2</sup>, X. Sun<sup>1</sup>, A. Hagen<sup>1</sup>

<sup>1</sup> Department of Energy Conversion and Storage, Technical University of Denmark, Risø, Roskilde, 4000, Denmark

<sup>2</sup> Hybrid Greentech ApS, Risø, 4000, Denmark

Received December 11, 2018; accepted May 23, 2019; published online July 18, 2019

## Abstract

In the renewable energy scenario, energy storage is of essence. In this context, power-to-liquid (PtL) and power-to-gas (PtG) concepts have attracted large attention, where the use of solid oxide electrolysis cells (SOECs) has a huge potential, due to their high conversion efficiencies. However, performance and durability of these cells still need to be improved for a large-scale commercialization of the SOEC technology. It is often difficult to identify the various loss and degradation mechanisms limiting the cell performance and durability. This paper contributes to this scientific discussion, by providing a careful analysis of the degradation mechanisms occurring in three different cells during long-term H<sub>2</sub>O and CO<sub>2</sub> co-electrolysis, at 1,200 mV. Electrochemi-

cal impedance spectroscopy (EIS) is measured before, during and after the electrolysis operation, and is utilized to address the individual electrode degradation mechanisms and the development of leaks through the electrolyte. Moreover, the leak rates under open circuit voltage (OCV) measurements were compared. In addition, microstructural analysis of the electrodes and electrolytes is related to the electrochemical findings to contribute to the discussion on the interdependency of the degradation mechanisms.

**Keywords:** Co-electrolysis, Distribution of Relaxation Times, Durability, Electrochemical Impedance Spectroscopy, Infiltration, Nickel Migration, Percolation, Potentiostatic, Solid Oxide Electrolysis Cell

## 1 Introduction

Renewable energy sources are gaining importance for energy production worldwide. For instance, in the case of Denmark, almost 50% of electricity production is currently provided by wind turbines and the transition towards 100% is expected to occur by 2050 [1]. Due to the intermittency of renewable energy sources, such as solar and wind, storage of electricity is of essence. Furthermore, there is an increasing need for production of renewable fuels for the transport sector. In this context, SOECs can play a major role for PtG and PtL applications, by the means of co-electrolysis of H<sub>2</sub>O and CO<sub>2</sub> to synthesis gas (H<sub>2</sub> + CO), and further on to hydrocarbons

[2–7]. One of the promising scenarios is to use SOECs for methane production, which can be stored and distributed in the existing natural gas infrastructure [8].

However, the performance and durability of SOECs need to be improved further, to realize a successful commercialization [7, 9–12]. Satisfying durability is, in particular, a challenge if the cells are operated at high current density [13]. SOECs, in this work, refer to the fuel electrode supported cell configuration. Degradation of the cermet of nickel and yttria stabilized zirconia (Ni:YSZ) active layer, is typically related to microstructural changes such as coarsening of Ni particles, migration of Ni par-

[\*] Corresponding author, [mrao@dtu.dk](mailto:mrao@dtu.dk)

 This is an open access article under the terms of the Creative Commons Attribution-NonCommercial License, which permits use, distribution and reproduction in any medium, provided the original work is properly cited and is not used for commercial purposes.

<sup>▲</sup> Paper presented at the 13th EUROPEAN SOFC & SOE Forum (EFCF2018), July 3–6, 2018 held in Lucerne, Switzerland. Organized by the European Fuel Cells Forum [www.efcf.com](http://www.efcf.com)

titles away from fuel electrode adjacent to the electrolyte, decrease in the Ni:YSZ contact area, and loss of percolation of Ni particles [14]. The irreversible microstructural degradation during the long-term tests might relate to the impurities in the gas stream [15,16]. Another contributor to the area specific resistance (ASR) of the cell is the oxygen electrode, through the oxygen electrode activity [17,18]. A vast number of routes to address these challenges are currently being investigated [19]. This includes improvement of the oxygen electrode through backbone infiltration [20,21], and optimization of the particle size, porosity and percolation in the Ni:YSZ electrodes [10].

In this work, a state-of-the-art (SoA) cell (Cell-A) was tested as a reference. The work performed in this study was to enhance the performance of this SoA cell. This was done by modifications of the electrodes and resulted in Cell B and C. Two modified cells comprising of (i) a cell with a gadolinium doped ceria (CGO) oxygen electrode backbone structure with lanthanum strontium cobaltite (LSC) infiltrated into the backbone (Cell-B) and, (ii) a cell with modified fuel electrode structure and an LSC-CGO composite oxygen electrode (Cell-C), were tested for initial performance and long-term durability in co-electrolysis mode, and compared to Cell-A. This work analyzes the electrochemical performance of the cells and compares the impact of the electrode modifications.

## 2 Experimental

Three different types of SOECs were tested in this study, as shown in Figure 1.

Cell-A, a state-of-the-art cell, is used as a reference cell. It has a 40–60  $\mu\text{m}$  lanthanum strontium cobalt ferrite-gadolinium doped ceria (LSCF-CGO) oxygen electrode, a CGO barrier layer, a 6–10  $\mu\text{m}$  thick YSZ electrolyte, and a 220–260  $\mu\text{m}$  thick Ni:YSZ fuel electrode, which also serves as support layer. Cell-B has a 30  $\mu\text{m}$  thick CGO backbone layer, in which LSC was infiltrated, a 6–7  $\mu\text{m}$  thick CGO barrier layer, a 10  $\mu\text{m}$  thick YSZ electrolyte, a 12–16  $\mu\text{m}$  thick Ni:8YSZ fuel electrode and a 300  $\mu\text{m}$  thick Ni:3YSZ support layer. For infiltration of LSC into the CGO backbone, 1M solution of LSC was used, and the cell was heat treated at 350  $^{\circ}\text{C}$  after infiltration. This

procedure was repeated 9 times to establish sufficient LSC solid loading in the CGO backbone. Cell-C has a 30  $\mu\text{m}$  thick composite LSC-CGO oxygen electrode, similar barrier layer, electrolyte and support as Cell-B, and a fuel electrode optimized by densifying the fuel electrode to obtain 22% porosity after NiO reduction. The cell fabrication method is published elsewhere [10]. The active area of the cells was 16  $\text{cm}^2$ .

The cells were tested in a previously described test setup [22,23]. They were mounted on an alumina cell test house with gold and nickel as current collector contact components on the oxygen and fuel side, respectively. A gold sealing was used on the fuel side. 4 kg of weight was applied on top of the cell house during start up to ensure gas tight sealants and electrical contact between the cell and the contact components. Cell-A was heated to 800  $^{\circ}\text{C}$  at a ramp rate of 60  $^{\circ}\text{C h}^{-1}$  and held for 2 h prior to reduction. During heating,  $\text{N}_2$  and air were supplied to the fuel electrode and oxygen electrode compartment, respectively. The cell was reduced with  $\text{N}_2$  and  $\text{H}_2$  beginning from 90%  $\text{N}_2$  for 1 h, eventually shifting the flow to pure  $\text{H}_2$  for 1 h on the fuel electrode. Cell-B and Cell-C were heated to 850  $^{\circ}\text{C}$  at a ramp rate of 60  $^{\circ}\text{C h}^{-1}$  and held for 2 h prior to reduction. During reduction, a mixture of 9%  $\text{H}_2$  in  $\text{N}_2$  was supplied to the fuel electrode. Cell-A is a commercial SoA cell while B and C are produced in-house. Cell-A is reduced at 800  $^{\circ}\text{C}$  as per manufacturer's protocol and the other two cells made in-house need to be reduced at 850  $^{\circ}\text{C}$ . In order to achieve best performance and durability, the cells need to be reduced at the optimized temperature for the specific cell types. On the oxygen electrode, a constant air flow of 140 normal liter per hour was maintained. Initial electrochemical characterization (fingerprint) of the cell was performed afterwards.

The fingerprint is a standardized electrochemical characterization of the cells at 800  $^{\circ}\text{C}$ , 750  $^{\circ}\text{C}$ , 700  $^{\circ}\text{C}$  and 650  $^{\circ}\text{C}$ . At each temperature,  $I$ - $V$  characterization and EIS measurements were performed with air or  $\text{O}_2$  supplied to the oxygen electrode, and with 4%, 20%, 50%, 80%, or 90% steam in  $\text{H}_2$  to the fuel electrode. Furthermore, characterization in co-electrolysis gas mixture was carried out with 45%  $\text{H}_2\text{O}$  + 45%  $\text{CO}_2$  + 10%  $\text{H}_2$  or 65%  $\text{H}_2\text{O}$  + 25%  $\text{CO}_2$  + 10%  $\text{H}_2$  supplied to the fuel electrode.

EIS measurements during fingerprint were carried out at OCV condition, using a Solartron 1255 frequency analyzer and an external shunt resistor in series with the cell. The spectra were recorded from 96,850 to 0.08 Hz, with 12 points per decade, and were corrected using the short circuit impedance response of the test setup. A short circuit impedance response for compensation of EIS was measured without the cell test house. From the impedance spectra, the ohmic resistance of the cell (serial resistance,  $R_s$ ) was taken as the value of the real part of the impedance at 96,850 Hz. Conventionally, the  $R_s$  is obtained from the intercept of the  $Z'$ -axis. However, as previously reported by Sun et al. [7], the calculation of  $R_s$  performed in this work provides a more precise value. The difference between the

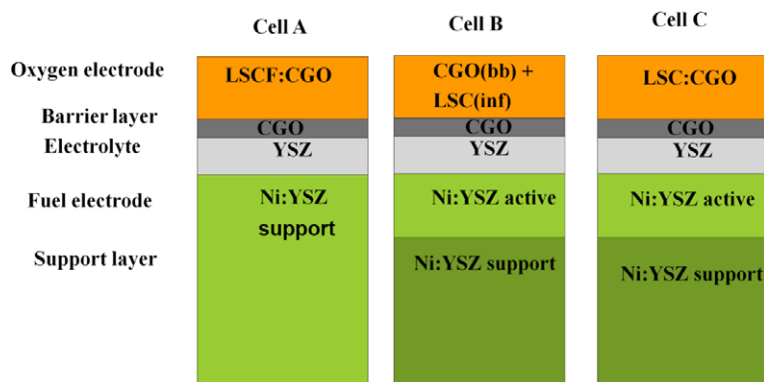


Fig. 1 Schematic representation of fuel electrode supported cells with the composition of layers.

intercept and this value is indeed very small. The polarization resistance ( $R_p$ ) was then calculated as the difference of the real part of the impedance at 96,850 Hz and 0.08 Hz. EIS measurements during durability tests were carried out at 1.2 V.

$I$ - $V$  curves were recorded both in fuel cell (FC) and electrolysis (EC) mode with the above-mentioned gas compositions. For FC mode, the minimum voltage limit was set to 650 mV while for EC mode the curve maximum voltage was set to 1,300 mV. The  $I$ - $V$  curves were recorded in 3 parts with step sizes of firstly 0.25 A, followed by 0.5 A in the linear region, and finally 0.25 A. The step size of 0.25 A was maintained, until either the current or voltage threshold was reached.

The electrochemical durability testing of the cells was carried out at 750 °C in co-electrolysis mode with 65%  $H_2O$  + 25%  $CO_2$  + 10%  $H_2$  in the fuel feed corresponding to a theoretic thermodynamic equilibrium composition of 23%  $CO_2$  + 2%  $CO$  + 8%  $H_2$  + 67%  $H_2O$ . The voltage was kept constant at 1.2 V, with varying current densities throughout the durability testing, as a consequence of degradation [24]. Cell A and Cell-C were tested for 1,000 h, while Cell B for 500 h. Analysis of the impedance data was performed using the software Ravдав [25]. The overall test sequence is presented in Figure 2.

Post-test analysis of the cells was performed using scanning electron microscopy (SEM). Polished cross-sections along the hydrogen/steam flow path from inlet to outlet were prepared for all cells. The cell microstructure was examined using a Supra-35 SEM equipped with a field emission gun (FE-SEM, Carl Zeiss) and an energy dispersive X-ray spectrometer (EDS, Thermo Electron Corporation). For SEM imaging, low voltage (LV) SEM through an In-lens detector at an accelerating voltage of 1 keV was employed [26]. The samples were embedded in epoxy and carbon coated to avoid charging of the sample surface and to ensure a grounded connection. Fractured samples were prepared from hydrogen inlet to outlet and were carbon coated for analysis. In-lens and SE detectors were used at 5 keV to investigate the surface morphology of these samples. EDS analysis was carried out at 10 keV for elemental analysis.

## 3 Results and Discussion

### 3.1 Overview of Electrochemical Performance

The three cells were characterized, and their initial performance is compared in Figure 3 under co-electrolysis conditions, with 65%  $H_2O$  + 25%  $CO_2$  + 10%  $H_2$  to the fuel electrode

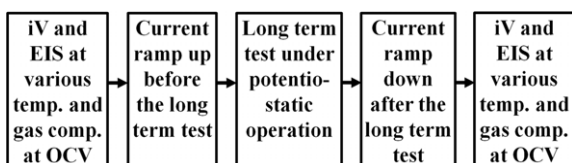


Fig. 2 Scheme representing the methodology for evaluation of test results.

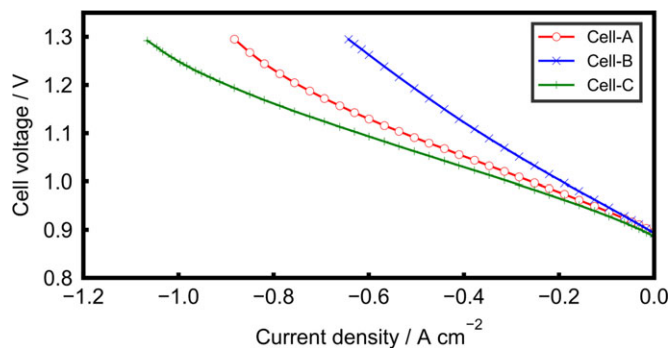


Fig. 3  $I$ - $V$  curves during initial characterization under co-electrolysis conditions with 65%  $H_2O$  + 25%  $CO_2$  + 10%  $H_2$  to fuel electrode and  $O_2$  to oxygen electrode, at 750 °C; Cell A: SoA, Cell B: Cell with modified oxygen electrode, Cell C: Cell with modified fuel electrode.

and  $O_2$  to the oxygen electrode, at 750 °C. The OCV values for the cells are similar, however they deviate from the theoretical value, in the range of 1–3%. This indicates the presence of leaks in the test, which will be addressed later in this work.

Taking the Cell-A as reference, Cell-C performed better while Cell-B performed worse as can be seen from Figure 3. Cell-A and Cell-B performed similarly at low current densities, up to 0.2  $A\ cm^{-2}$ . Thereafter, the performance of Cell-B deviated from Cell-A. Cell-C performed significantly better than the other two cells from the beginning. By modifying the oxygen electrode using the backbone/infiltration concept, a decrease of initial performance was observed, while by modifying the fuel electrode in terms of structure, a significant increase of performance was observed.

Owing to the difference in initial performance, the operational parameters for testing of long-term durability were determined. The selection of testing conditions was based on the project goals of the EU-ECo project; cells were tested at 1,200 mV and 750 °C under co-electrolysis conditions. The overpotentials of the cells under durability testing were calculated for the tests in this study as [12]:

$$Op = U - OCV - I R_s \quad (1)$$

where  $Op$  is the cell overpotential,  $U$  is the cell voltage,  $OCV$  is the open circuit voltage,  $I$  is the current density and  $R_s$  is the serial resistance.

In this calculation, the contribution from the serial resistance is excluded to analyze the overpotential of only the electrodes. At an operating voltage of 1,200 mV, current densities of 0.6  $A\ cm^{-2}$  for Cell-A, 0.33  $A\ cm^{-2}$  for Cell-B and 0.8  $A\ cm^{-2}$  for Cell-C were obtained from the  $I$ - $V$  curves. Following this,  $R_s$  and  $OCV$  (including leaks) were obtained, and the overpotential of the electrodes thus obtained are displayed in Table 1. The cells experienced similar electrode overpotentials. Furthermore, the long-term operation was carried out under potentiostatic conditions, and the overpotentials are similar at the beginning and end of this testing period.

In Figure 4a, the evolution of current density during the long-term tests is shown. Note, that a degradation under

Table 1 Overpotential at the beginning and end of durability testing.

Test	Rs at the beginning of the long-term test / $\Omega \text{ cm}^2$	Overpotential at the beginning of the long-term test / mV	Rs at the end of the long-term test / $\Omega \text{ cm}^2$	Overpotential at the end of the long-term test / mV
Cell-A	0.154	329	0.157	324
Cell-B	0.199	317	0.208	313
Cell-C	0.134	317	0.151	318

where OCV is the open circuit voltage measured experimentally,  $U$  is the measured cell voltage, and  $I$  is the measured current density.

The OCV used for ASR calculation is the one measured prior to the long-term test. This OCV change will be further discussed, in relation to the results on changes in electrode microstructure and resistance.

The ASR evolution for the cells is shown in Figure 4b. The general trends are comparable to those observed with the current density. Regardless of the difference in the initial ASR values, Cell-A and Cell-B show similar degradation behavior. In the first 200 h, a high rate of degradation of ASR is observed followed by a more gradual/stable lowering of the rate of degradation. For Cell-C, a different trend is observed which is more linear in nature and the overall rate of degradation is smaller than the other two cells. The high initial degradation of SoA cells was significantly reduced in this manner and the overall degradation rate as well. The high initial degradation of Cell-A was reduced due to difference in the cell structure with regard to modification done for Cell-C and the overall degradation rate as well. It should be taken into account that the initial ASR for Cell-C was the lowest amongst the cells, therefore Cell-C was exposed to a significantly higher current density at the beginning of the test, which might affect the degradation mechanisms as well. The ASR is calculated using the measured OCV values, which is different among the cells. However, the aim of this work is to determine the change in ASR to understand the underlying mechanisms clearly. As a change of ASR can be used as an indicator which can be analyzed relatively before and after durability test, the mechanisms can be deconvoluted.

Following the ASR and EIS evolution during testing, the behavior of serial ( $R_s$ ) and polarization ( $R_p$ ) resistances was investigated in more detail, because the cells displayed different degradation behavior. Previous studies have used normalized  $R_p$  vs.  $R_s$  plots to identify degradation mechanisms, e.g., Gazzari and Kesler [27]. In such a way, phenomena like delamination of layers or structural degradation can be distinguished. Figure 5 shows the  $R_p$  vs.  $R_s$  plots for the cells in this study. A vertical line from point (1,1) is a result of the dominance of  $R_p$  changes as compared to  $R_s$ , which might be caused by structural changes in the electrodes, such as nickel coarsening, chromium poisoning and/or changes due to steam content on the oxygen electrode [28]. A horizontal line from point (1,1) shows the dominance of increase of  $R_s$  over  $R_p$ , for instance due to oxide layer growth. If the values follow the 45° slope, a loss of active area is indicated [28]. For Cell-A, the values seem to increase vertically from point (1,1) indicating only  $R_p$  increase, while for Cell-B both increase:  $R_p$  and to a certain extent also  $R_s$  in combination with  $R_s$  as seen from Figure 5. This is an indication of at least two different degradation mechanisms. For Cell-C, the plot follows the 45° slope, i.e., a parallel increase of  $R_s$  and  $R_p$  happens, indicating one

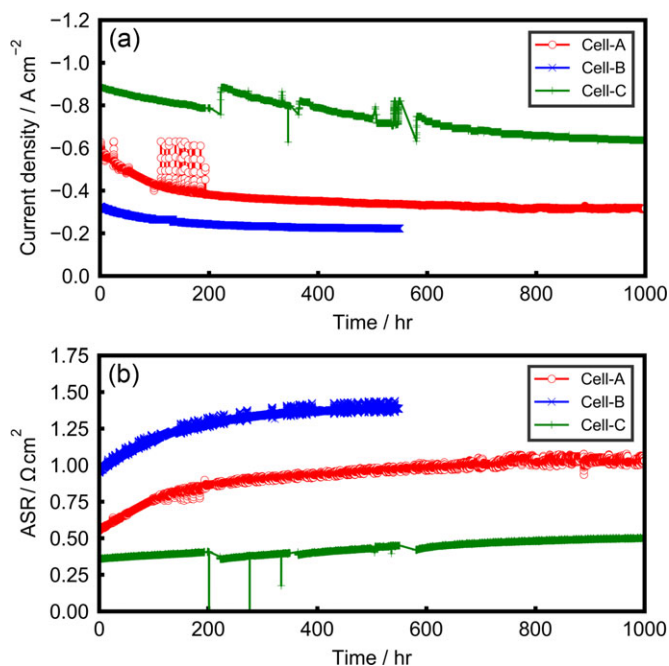


Fig. 4 (a) Evolution of current density over time, and (b) Evolution of ASR under long term testing, with 65%  $\text{H}_2\text{O}$  + 25%  $\text{CO}_2$  + 10%  $\text{H}_2$  on fuel electrode and  $\text{O}_2$  on oxygen electrode, at 750 °C (Note: The jumps of the current density for Cell-A were due to technical problems of the potentiostatic control for the cell operation, particularly between 100–200 h of the test. Similar issues were observed for Cell-C between 200–400 h); Cell A: SoA, Cell B: Cell with modified oxygen electrode, Cell C: Cell with modified fuel electrode.

potentiostatic SOEC conditions is reflected in a decrease of current density over time. For the long-term tests, the current densities of the three cells at the start of the test varied significantly for the three cells, as expected from the initial  $I$ - $V$  curves depicted in Figure 3. Following Table 1, however, the overpotentials at 1,200 mV are comparable and the change of the current density relative to the start of the test for each cell are traced. For Cell-A, there was a higher degradation in the initial 200 h. The same trend is observed for Cell-B. This behavior has been observed on different types of SoA cells [10]. However, for Cell-C, the trend of degradation rate was linear throughout the durability test and the rate of degradation over the 1,000 h of testing remained almost constant.

To further understand the degradation and compare the three long-term tests, area specific resistances (ASR) were calculated using the following equation:

$$\text{ASR} = (\text{OCV} - U)/I \quad (2)$$

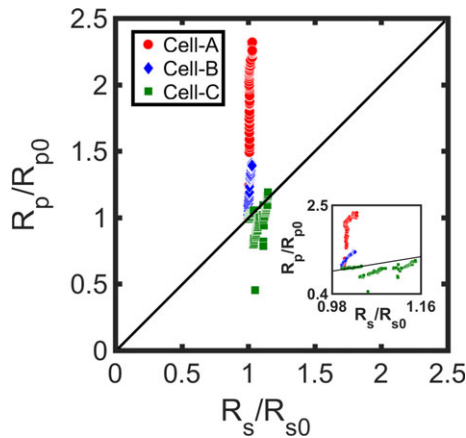


Fig. 5 Normalized  $R_p$  vs.  $R_s$  plots for long-term testing (inset: zoomed in image showing different degradation trends); Cell A: SoA, Cell B: Cell with modified oxygen electrode, Cell C: Cell with modified fuel electrode;  $R$  values were taken during operation.

dominant degradation mechanism, but a different one from Cell A. This gives an indication of different degradation mechanisms occurring in the cells. These findings will be further investigated using EIS results.

### 3.2 Electrochemical Impedance Analysis

To investigate the evolution of the cell performance during long-term testing, the impedance spectra are plotted with increasing time in Figure 6 for all three cells. In Figure 6a, the

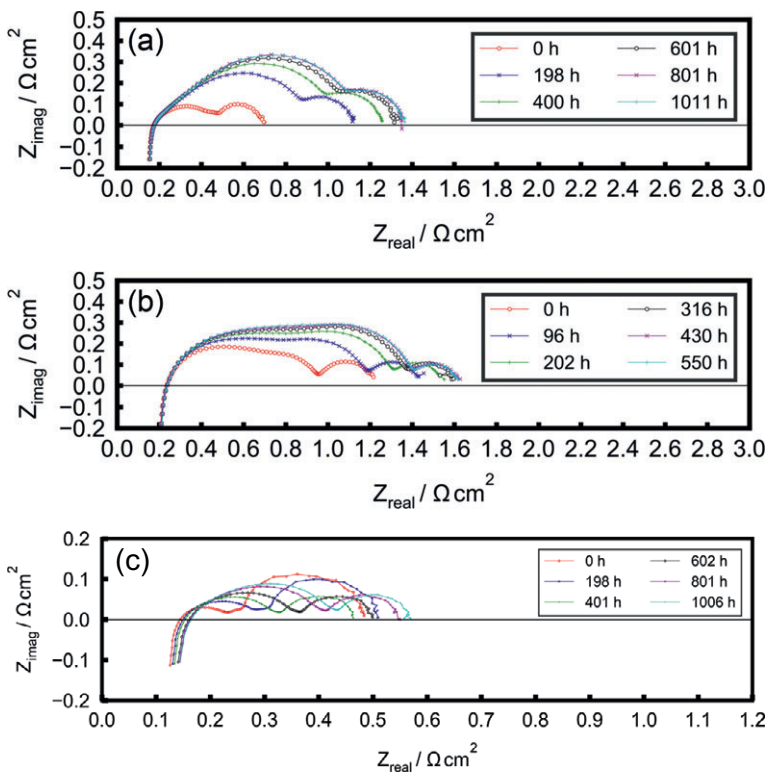


Fig. 6 EIS over long-term testing for (a) Cell-A, (b) Cell-B, and (c) Cell-C.

evolution of impedance from 0 h to 1,000 h is plotted every 200 h for Cell-A. It is evident that there is no change in the serial resistance ( $R_s$ ) while the polarization resistance ( $R_p$ ) keeps increasing. However, it should be noted that the current density is not constant throughout the test, and a direct comparison of degradation mechanisms is not possible due to the change of the contribution of the gas conversion resistance as consequence of the changing current density. For the case of Cell-B in Figure 6b, similar influence on  $R_s$  and  $R_p$  are observed. In addition, a small increase of  $R_s$  occurred as seen from Table 1 and Figure 5. For Cell-C, the evolution of EIS over time shows a completely different trend than the other two cells as shown in Figure 6c. An increase in  $R_s$  is observed which might be due to electrode degradation/cracks in the electrolyte. Furthermore,  $R_p$  is increasing to a certain extent. The increase in  $R_s$  can also be confirmed from the values given in Table 1. In total, the increase of impedance is smaller as compared to Cell-A and Cell-B, which is in line with the observation of the other parameters discussed above.

To further identify the source and extent of degradation, specific degradation mechanisms need to be investigated. This was done by using distribution of relaxation times (DRT) from EIS spectra [29]. From DRT analysis, contribution of individual electrodes is deduced. This is done by gas shift analysis, where EIS are recorded in differently composed gas mixtures to oxygen and fuel electrodes at OCV. By varying the steam content, while keeping the gas to the oxygen electrode constant, the response of the fuel electrode is distinguished in the EIS spectrum, at a specific frequency range. Similarly, while keeping the fuel flow/composition unchanged, and by changing only the oxygen partial pressure (shifting from oxygen to air), the response of the oxygen electrode is noted. The characteristic frequencies identified by DRT for the individual electrode processes are given in Table 2.

For Cell-A there is an overlap of electrode response for both fuel and oxygen electrode and hence the change of DRT for the individual electrodes was difficult to obtain. For Cell-B and Cell-C, the deconvolution of arcs with respect to the contribution from individual electrodes was possible. However, to strengthen the identification, the DRT was also analyzed prior to the durability testing when the current was ramped up and down, respectively, to better resolve the electrode contributions. Furthermore, during and after the test, DRT analysis also rendered useful information. DRT plots are displayed for each cell from beginning until the end of the whole test in Figures 7–9, based on the characterization sequence illustrated in Figure 2.

In Figure 7, the responses of individual electrodes for Cell-A are mapped over the whole test. DRT analysis during the initial fingerprint is not sufficiently resolved to distinguish the contributions of fuel and oxygen electrodes, as seen in Figures 7a and 7b. There is an overlap in the frequency of these pro-

Table 2 Identification of electrode processes through DRT gas shift analysis.

Process	Relaxation frequency		
	Cell-A	Cell-B	Cell-C
1 Gas conversion	1–3 Hz	1–3 Hz	1–3 Hz
2 Diffusion	30–50 Hz	30–50 Hz	30–50 Hz
3 Oxygen electrode	100–1,000 Hz, 1–8 kHz	500–1,500 Hz	100–200 kHz
4 Fuel electrode, triple phase boundary (TPB) processes	100–1,000 Hz, 1–8 kHz	3–5 kHz	1–3 kHz
5 Fuel electrode, oxygen ion transport	18–20 kHz	10–20 kHz	8–10 kHz

cesses, from 100 Hz–8 kHz, as reported earlier [30]. There is an additional response from a fuel electrode process, at approximately 10–20 kHz. However, it is interesting to see the trend of degradation with ramping up of current. These two processes seem to move towards decreasing frequency, as seen from Figure 7c. Moreover, during long-term testing, the two processes seem to merge, and are seen in the form of a single arc in DRT spectrum shown in Figure 7d. This indicates that both the electrodes degrade over time. Furthermore, during the ramping down of current after the durability test as shown in Figure 7e, the processes can be seen separated at OCV, but the summit frequencies have decreased. It was of interest to deconvolute the mechanisms after the long-term testing. DRT plots for fuel and oxygen electrode shifts are plotted with respect to the final fingerprint in Figures 7f and 7g. The two processes appear to overlap around 500 Hz. However, the contribution from the oxygen electrode has increased significantly as compared to the initial fingerprint, while the fuel electrode contribution increased slightly from the initial fingerprint. The magnitude of degradation of oxygen electrode is quite high as compared to the fuel electrode, which becomes obvious through the gas shift plots performed before and after the long-term test. This also indicates the presence of leaks. Regardless of the overlap of the frequencies, major contribution to the cell degradation is therefore attributed to the oxygen electrode ASR.

Similarly, the DRT plots for Cell-B are represented in Figure 8. Through initial fingerprint from Figures 8a and 8b, the deconvolution of individual electrode processes was possible with fuel electrode processes occurring at frequencies of 3–5 kHz and 10–20 kHz, while the oxygen electrode process was approximately around 500–1,500 Hz. During ramping-up of current in Figure 8c, the processes seem to move towards low frequency. Moreover, a clear distinction of the oxygen electrode process is seen under current. During the long-term test, the oxygen electrode degrades continuously, while the fuel electrode degradation is clearly visible until 400 h, in Figure 8d. The magnitude of degradation of oxygen electrode is significantly higher than the fuel electrode. This may be due

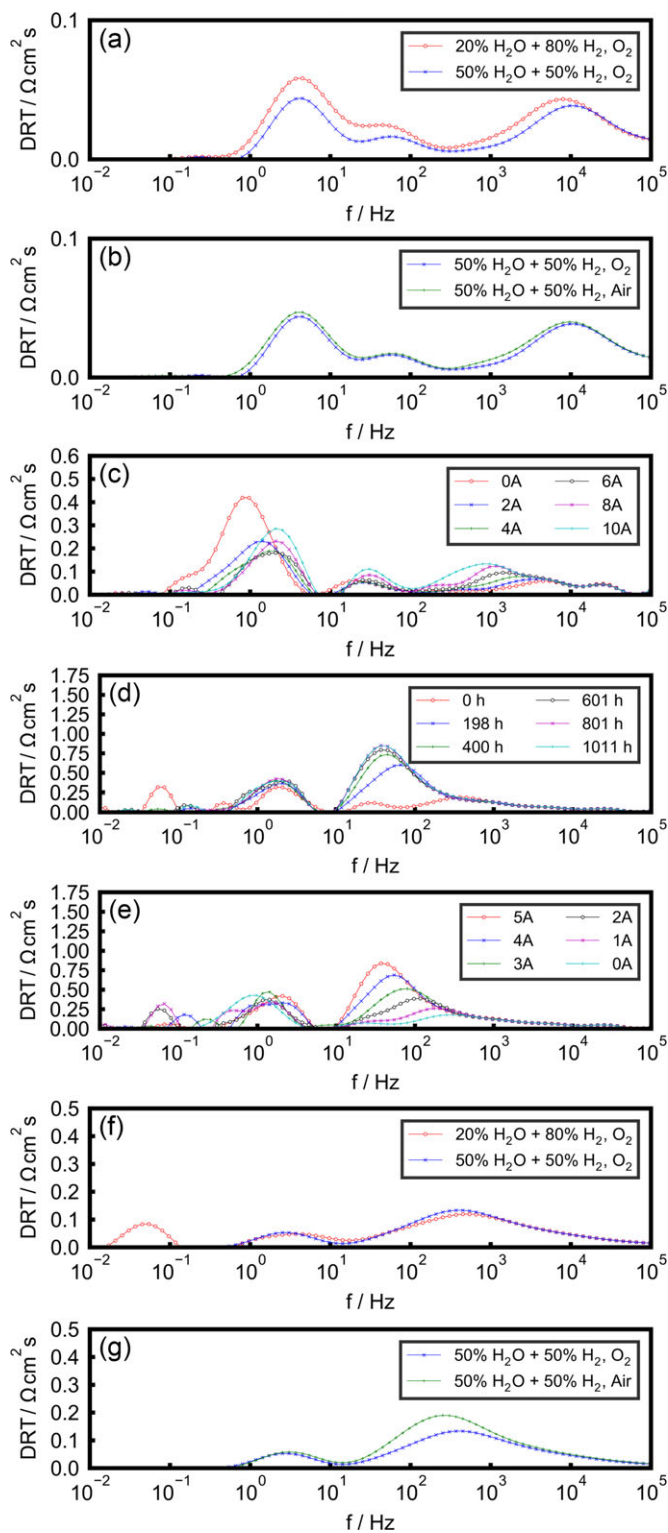


Fig. 7 DRT analysis of Cell-A (a) change in fuel electrode composition (initial fingerprint), (b) change in oxygen electrode gas composition (initial fingerprint), (c) current ramp-up, (d) during long-term test, (e) current ramp-down, (f) change in fuel electrode composition (final fingerprint), (g) change in oxygen electrode gas composition (final fingerprint).

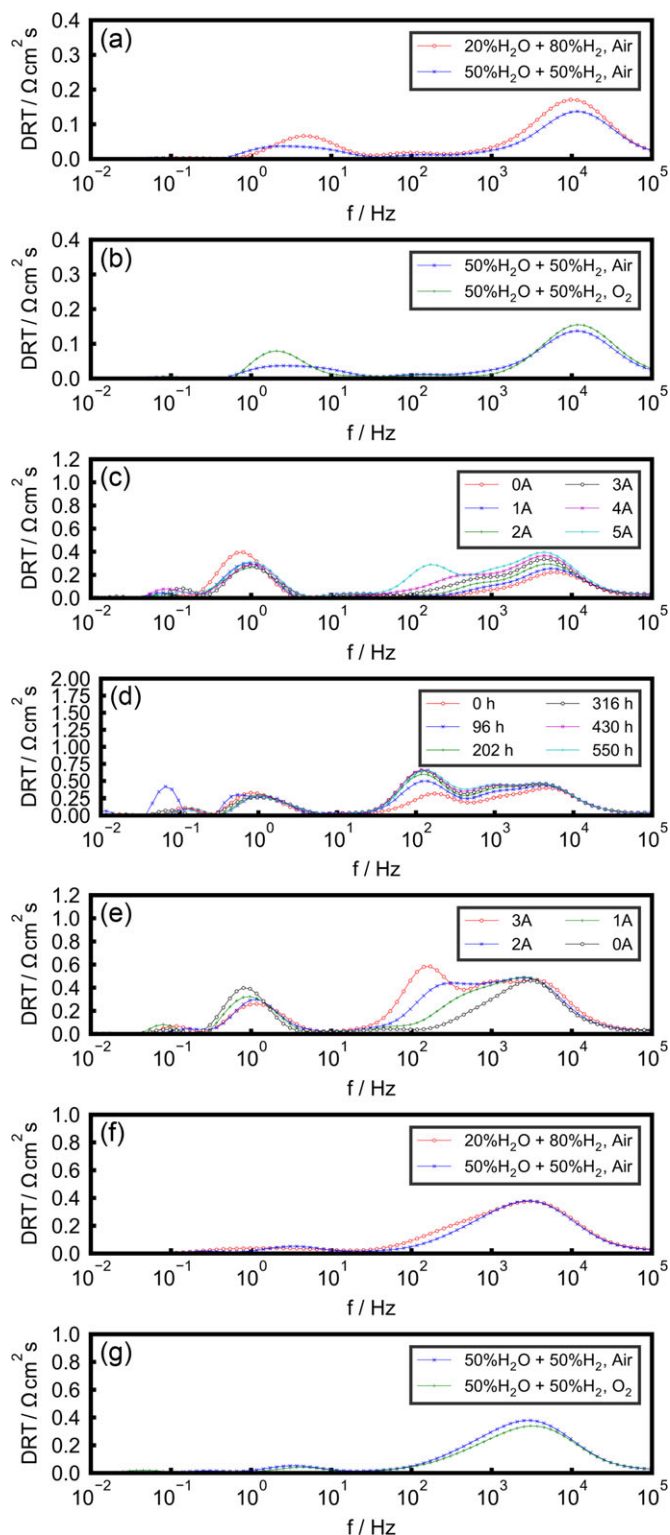


Fig. 8 DRT analysis of Cell-B (a) change in fuel electrode composition (initial fingerprint), (b) change in oxygen electrode gas composition (initial fingerprint), (c) current ramp-up, (d) during long-term test, (e) current ramp-down, (f) change in fuel electrode composition (final fingerprint), (g) change in oxygen electrode gas composition (final fingerprint).

to the non-optimized infiltration process of the CGO backbone with LSC solution, which has been further identified through SEM analysis. During ramping down of current as well as the final fingerprint, the deconvolution of arcs at OCV becomes difficult, as seen from Figures 8e, 8f, and 8g. This might be due to the severe degradation of the cell. Moreover, leaks were also present during the testing.

For the case of Cell-C, DRT plots are represented in Figure 9. Using initial fingerprint in Figures 9a and 9b, the response of oxygen electrode process is found around 100–200 kHz, while the fuel electrode processes occur around 1–3 kHz and 8–10 kHz. During ramp up of current, a shift towards lower frequencies is seen for the fuel electrode processes in Figure 9c. However, the conversion arc present at approximately 1 Hz dominates the DRT spectrum and the electrode processes are not clearly visible, i.e., the arc at 1 Hz is significantly larger in magnitude around  $0.4 \Omega \text{ cm}^2$  while the processes have a magnitude of approximately  $0.05 \Omega \text{ cm}^2$ . During long-term testing, an increase in fuel electrode response is visible in Figure 9d. Furthermore, during ramping down of current as shown in Figure 9e, a similar trend is observed as in ramping up of current as seen from Figure 9c, however, the magnitude of fuel electrode response has increased. Moreover, from the final fingerprint, deconvolution of fuel and oxygen electrode processes is difficult indicating the cell degradation and increase in leaks.

From the DRT analysis over the whole testing period, Cell-A and Cell-B seem to degrade mainly due to the oxygen electrode. For explaining the degradation mechanisms, it is valuable to distinguish between the total overpotentials and the overpotentials experienced by the single electrodes. Even though the total overpotentials of the different cells might be similar, the distribution between the electrodes can differ and thus cause different degradation mechanisms. From Figures 7g and 8g, the DRT shows the magnitude of oxygen electrode response which is twice for the case of Cell-B when compared to Cell-A. The overpotential experienced by oxygen electrode in Cell-B is higher than that of Cell-A, hence, lowering the performance of Cell-B. For the case of Cell-C, the oxygen electrode is reasonably good and the overpotential experienced by the fuel electrode is higher than in the other two cells. This leads to a different degradation trend as revealed through electrochemical analysis.

To further emphasize on the leaks during testing, OCV values were used. The difference in OCV between the theoretical and measured value was related to the excess  $\text{O}_2$  gas leak into the fuel stream. The calculated difference in leaks indicate the extent of growth of leaks leading to cracks/delamination, if any. Note: All flows are in  $\text{NL h}^{-1}$ . To calculate the leak current, following equations are used:

$$\text{Number of moles} = \frac{\text{excess O}_2 (\text{L h}^{-1})}{22.4} \quad (3)$$

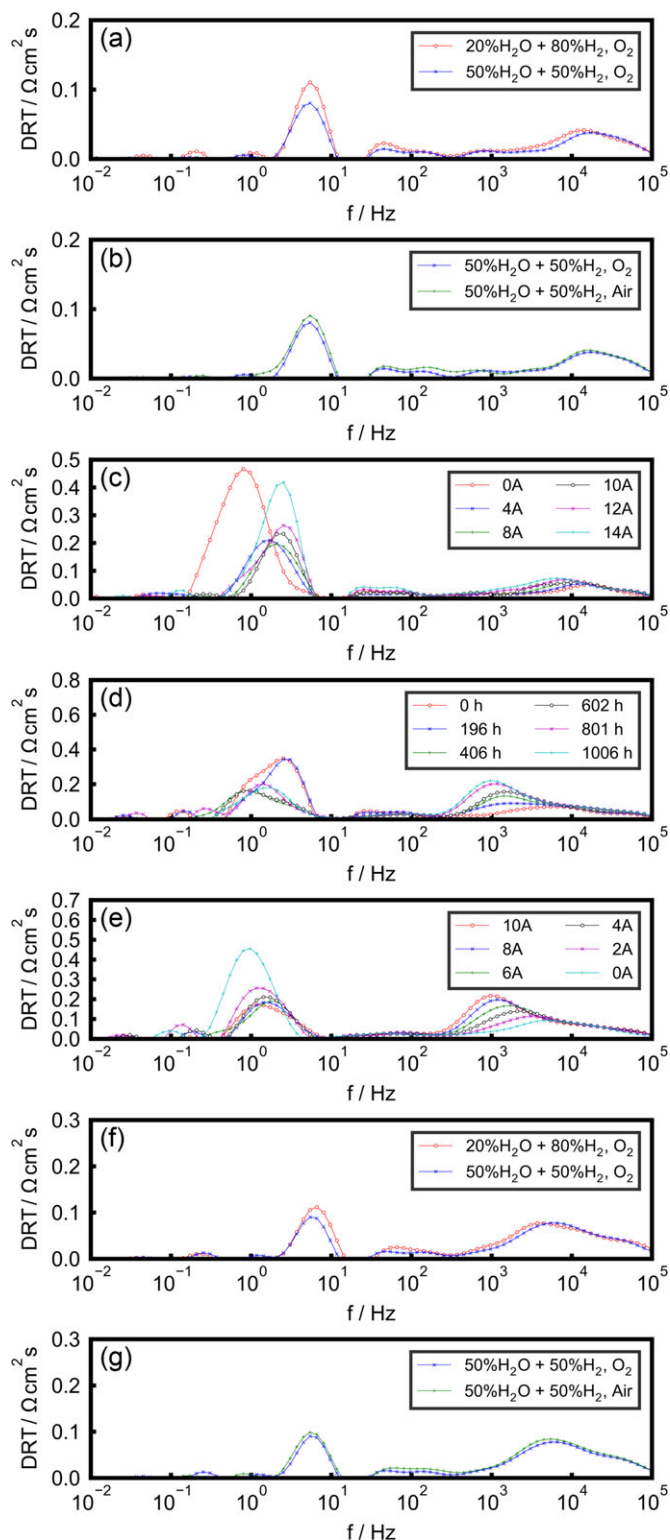


Fig. 9 DRT analysis of Cell-C (a) change in fuel electrode composition (initial fingerprint), (b) change in oxygen electrode gas composition (initial fingerprint), (c) current ramp-up, (d) during long-term test, (e) current ramp-down, (f) change in fuel electrode composition (final fingerprint), (g) change in oxygen electrode gas composition (final fingerprint).

Table 3 Calculation of leaks in the cell setup (50% H<sub>2</sub>O + 50% H<sub>2</sub> at the fuel electrode, O<sub>2</sub> at the oxygen electrode, at 750 °C).

Cell	Difference in OCV before / mV	Difference in OCV after / mV	Corresponding leak current before / mA cm <sup>-2</sup>	Corresponding leak current after / mA cm <sup>-2</sup>
Cell-A	25	25	90	90
Cell-B	6	12	45	67
Cell-C	12	23	67	90

$$\text{Leak current} = \frac{\text{Number of moles} (\text{mol h}^{-1}) \cdot F (\text{A s mol}^{-1}) \cdot 4}{3,600 \cdot 16 \text{ cm}^2} \quad (4)$$

where  $F$  is the Faraday constant, and 4 refers to the number of electrons per mole of excess O<sub>2</sub> gas.

It can be seen from Table 3 that the leaks change significantly for Cell-B and Cell-C during testing. Cell-C is of special interest because this cell was operated at significantly higher current densities than the other two cells. The difference of measured to theoretic OCV changed by 10 mV during the test. As a result, the overpotential experienced by the fuel electrode will be even higher than if no leaks were present. If the cell had no leaks, the OCV measured would be higher leading to difference between operating potential and OCV being lower. The impact of leak on Cell-C degradation and increase in  $R_s$  will be further addressed through microstructural analysis, in the later part of this work. In addition, further information is given in Appendix A.

### 3.3 Microstructural Analysis

Once the electrochemical test was completed, SEM analysis was performed to investigate structural changes and correlate them to the electrochemical results. The cells were investigated at 5 keV and 1 keV for morphology (oxygen electrode) using a SE-2 detector and at 1 keV for percolation studies [26] (fuel electrode) using the Inlens detector. In Figure 10, Cell-A, Cell-B and Cell-C are first compared to highlight the difference in the oxygen electrode structure. The oxygen electrode is on top, followed by the CGO barrier layer and the electrolyte. Cell-A consists of a composite LSCF-CGO oxygen electrode while Cell-B is prepared by infiltrating LSC solution into a CGO backbone and Cell-C consists of a composite LSC-CGO structure. Cell-A exhibits uniform particle size distribution throughout the electrode as seen from Figure 10a. For Cell-B, the areas adjacent to the CGO backbone show islands of LSC infiltrate instead of a continuous network of LSC nanoparticles as shown in Figure 11b. This indicates non-optimized infiltration. The non-optimized infiltration refers to the fact that a continuous network from the barrier layer to the oxygen electrode is considered to deliver high activity and thus a low area specific resistance. Instead, islands of infiltrates were observed. Such islands were also seen in a reference cell (sister

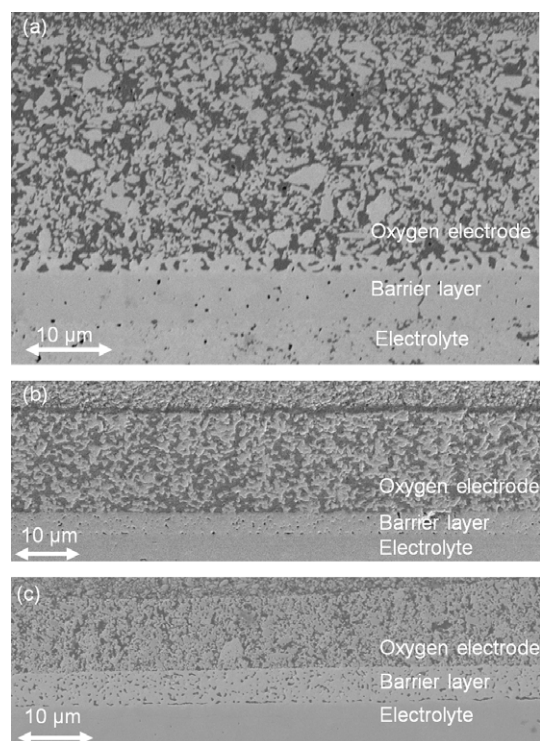


Fig. 10 SEM images for oxygen electrode comparison at 1 keV (a) Cell-A with LSCF-CGO composite electrode on top, followed by CGO barrier layer and YSZ electrolyte, (b) Cell-B with LSC infiltrated on CGO backbone on top, followed by CGO barrier layer, and (c) Cell-C with LSC-CGO composite electrode on top, followed by CGO barrier layer; cells after durability test.

cell to Cell-B), leading to the conclusion that the infiltrates were not forming a continuous network. This is displayed in Figure 11c. This results in higher ASR for the whole cell and lower performance. Cell-C consists of composite LSCF-CGO oxygen electrode.

An interesting aspect while comparing Cell-B and Cell-C relates to the CGO backbone for Cell-B, which seems to be very porous while the composite structure in Cell-C is denser. For Cell-B, even though there might be LSC particles surrounding the CGO backbone, the overall network of active sites is reduced as compared to Cell-C. This is further seen in Figure 11. Here, the images are taken at high magnification to assert the importance of combination of backbone and infiltration on the cell performance. LSC particles are clearly visible locally, for example indicated by the red circle in Figure 11b. However, the structure seems too coarse for the oxide ion conduction. This implies that there are infiltrates present around CGO backbone locally, however, the backbone itself is too coarse and the conduction path for the ions is reduced in this manner. The results indicate the inferior percolating capacity of the infiltrates for Cell-B. The infiltration technique can be further optimized to improve the performance of the cell. As a conclusion, the oxygen electrode structure overall is significantly inferior to Cell-A and Cell-C.

The other modification concept, fuel electrode improvement is investigated next. In Figure 12, the cells are compared

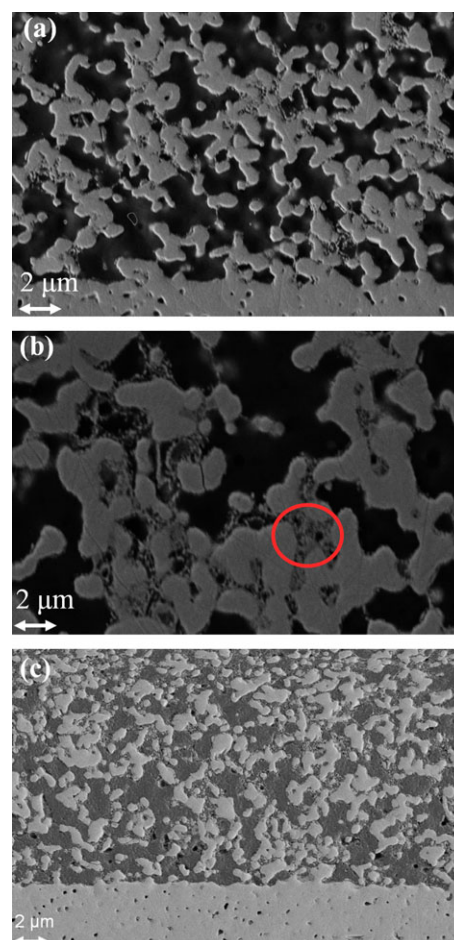


Fig. 11 SE-2 SEM images at 5 keV showing LSC infiltrates on CGO backbone for Cell-B (a) adjacent to the barrier layer, (b) zoomed in image showing local LSC infiltrates; cells after testing, (c) infiltrated sister cell to Cell-B, only tested for initial characterization.

such that the electrolyte is on top followed by the fuel electrode active layer and support. Moreover, bright particles in the fuel electrode represent percolating Ni [26]. Clearly, there is a significant difference in the porosity and particle size distribution for all three cells. For Cell-A, there is a uniform densely packed fuel electrode while for Cell-B and Cell-C, only the active layer is densely packed, but being more porous than Cell-A. For Cell-A and Cell-B, given that the cells operated at lower current density, the Ni network seems to be still percolating to a good extent. In Figure 12a, the fuel electrode of Cell-A shows a good percolation (bright spots towards the dark electrolyte) with a rather densely connected Ni network. During testing of Cell-A, cracks were observed only in post-mortem analysis. This has been investigated previously [30], wherein it was concluded that the cracks were not formed during the long-term testing, but afterwards. No change in OCV or Rs was observed during testing in this study, indicating that the cracks indeed were formed during final characterization. In Figure 12b, the same region also shows good percolation of Ni particles. In Figure 12c, percolated Ni particles of Cell-C are less in number when compared to Cell-B in the

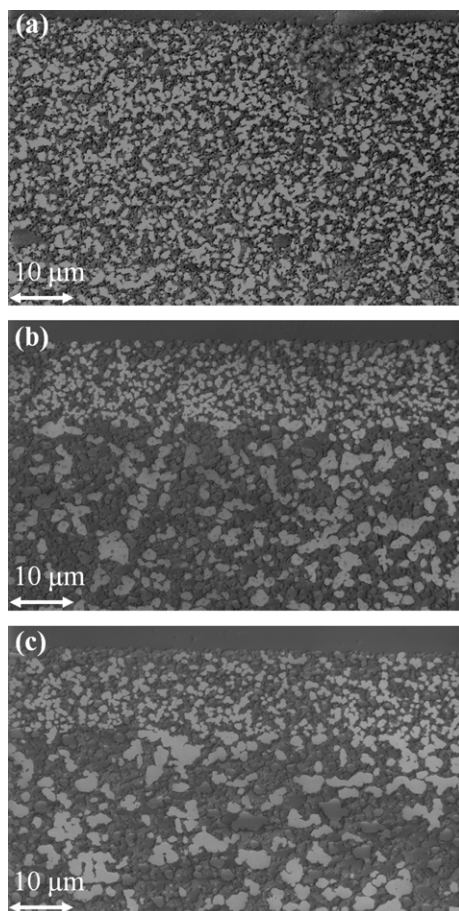


Fig. 12 SEM images at 1 keV for fuel electrode comparison (a) Cell-A with YSZ electrolyte on top, followed by Ni:YSZ electrode, (b) Cell-B and (c) Cell-C, with YSZ electrolyte on top, followed by Ni:YSZ active electrode and support; cells after testing.

active layer. The loss of percolation as a result of higher overpotential experienced by the cell is indicated.

To further assess the different effects of the fuel electrode overpotential for Cell-B and Cell-C, owing to their similar half-cell structure, the tested cells after long-term testing are compared to sister cells on which only fingerprint was performed. These are displayed in Figure 13. Loss in the Ni network is observed close to the electrolyte layer for Cell-B, as seen from the yellow circle in Figure 13a. For Cell-C, after long term testing at higher current densities than the other two cells, the loss of Ni percolation reaches a large extent. It is visible that Cell-C has lost significant amount of percolating Nickel after long-term test from Figure 13b, which is not the case for Cell-B.

It is interesting to recall that the  $R_s$  of Cell-C gradually increases over time. Moreover, this cell had the highest leak current amongst the three cells tested for durability. The change in  $R_s$  can be attributed to the loss of active area. To address this aspect, the microstructure of the cell with special emphasis on the electrolyte layer was investigated.

The delamination of the electrolyte layer is clearly visible in Figure 14. Grain boundary deterioration is observed in the

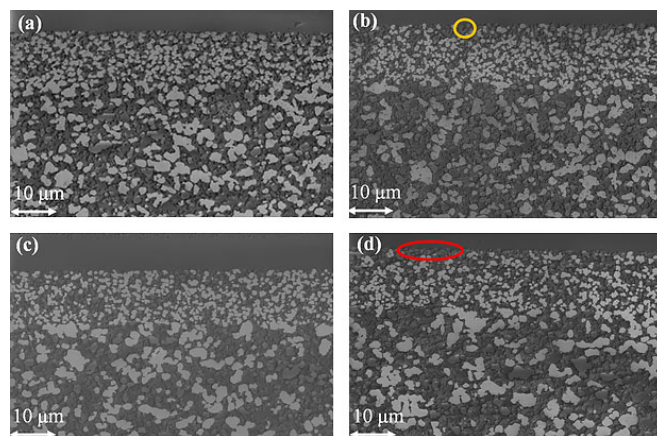


Fig. 13 LV-SEM images of fuel electrode (a) sister cell to Cell-B, only fingerprint test, (b) Cell-B after long-term test, (c) sister cell to Cell-C, only fingerprint test, and (d) Cell-C after long-term test.

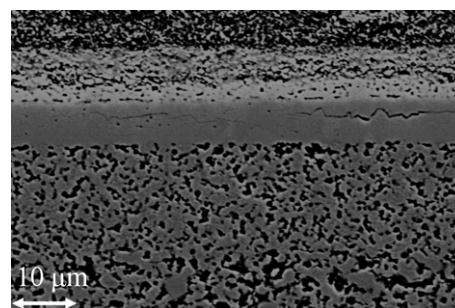


Fig. 14 Cell-C SEM displaying cracks in electrolyte after long-term testing.

electrolyte which indicates the weakening of interfaces due to high overpotential experienced by the cell, which is seen in *post mortem* analysis.

It is difficult to conclude the extent of influence of Ni migration or crack formation on the increase in  $R_s$ . Loss of percolation indicated the Nickel migration from the active layer to the support. Hence, it was also of interest to investigate the theory of Nickel migration [31]. For this purpose, line scans were done through Cell-C to check for the possibility of loss in Ni surface area due to migration. Figure 15 displays the difference in Ni content at the inlet, middle and the outlet of the reference cell (tested only for fingerprint) and the long-term tested cell. To obtain these plots, EDS line scan was performed close to the electrolyte in the active fuel electrode, as well as in the support layer near the active fuel electrode. The schematic representation is displayed in Figure 15a. The distance for the line scan is denoted in  $\mu\text{m}$ , with the distance being taken such that the interface between electrolyte and active fuel electrode is the reference. Inner active line scan was taken 1–2  $\mu\text{m}$  from this interface, along with outer active line scan being taken at 7–8  $\mu\text{m}$  from this interface and the support line scan being taken at 12–15  $\mu\text{m}$  from this interface. Thereafter, the counts are summed up and averaged. For further information, please refer to Appendix-B. This methodology gives an indication of

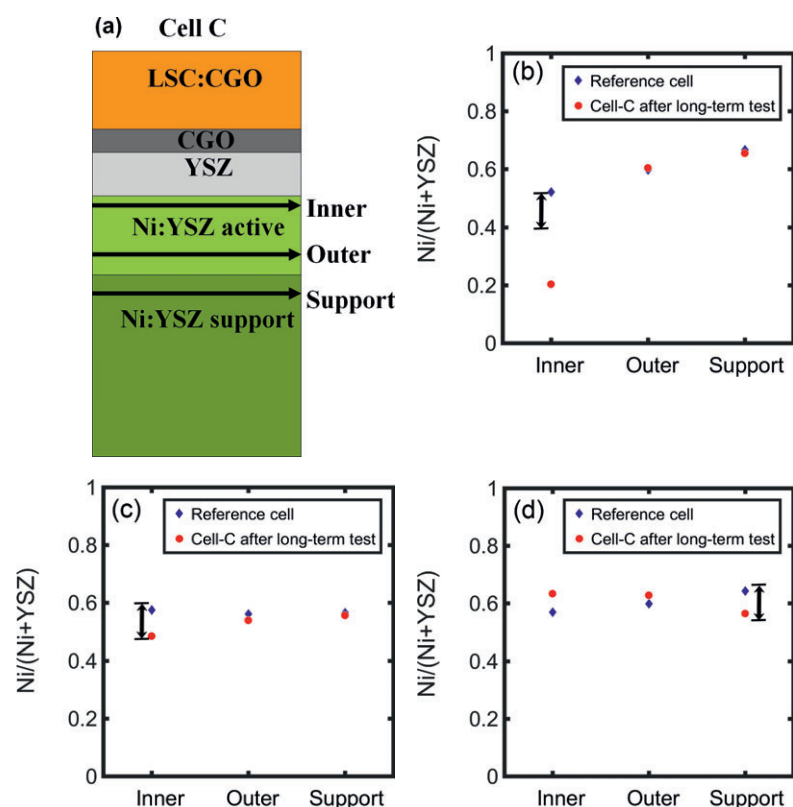


Fig. 15 (a) Schematic for EDS scan positions, Graphs displaying amount of Nickel in long-term tested cell, Cell-C (red circle) as compared to the reference cell, sister cell to Cell-C (blue diamond) at (b) inlet, (c) middle, and (d) outlet of the cell, with respect to the fuel flow direction (the double headed arrows indicate the error bar, i.e., the margin of error in analysis).

the magnitude of the Ni migration from the active region to the fuel support [31].

From Figure 15b, the inlet displays a lack of Nickel in the inner active electrode layer (i.e., at the electrode/electrolyte interface) while the outer layer as well as the electrode support display similar ratio of Ni/(Ni+YSZ), taking into account the error bar for the data analysis. However, for the case of middle and outlet of the cell the counts are almost similar in both reference and the long-term tested cell, within the margin of error. This explains qualitatively that Ni migration occurs predominantly at the inlet of the cell, where also the highest humidity is observed. Humidity has been reported earlier to favor the migration of Ni [31]. This asserts the fact that for Cell-C, degradation is due to Ni migration and resulting loss of percolation. Moreover, change in  $R_s$  is a result of Ni migration as reported by Mogens et al. [31]. Due to testing conditions, the deterioration of electrolyte and interfaces take place, leading to crack formation and increase in leaks. Further, crack formation due to leaks also causes an increase in  $R_s$ , which has been reported earlier [17].

## 4 Conclusions

The aim of the study was to reveal the different degradation behavior of the cells operated under co-electrolysis conditions with modified electrodes for durability at potentiostatic mode of operation and compare the performances with the SoA cell. Two concepts were investigated, namely (i) oxygen electrode modification by infiltrating LSC solution into a CGO backbone, and (ii) structural optimization in terms of porosity and particle size distributions in the Ni:YSZ fuel electrode. The cell with the infiltrated oxygen electrode showed a worse initial performance, and a larger degradation rate as compared to SoA. The main part of the cell overpotential was related to the oxygen electrode. The degradation was, therefore, mainly due to degradation of this part of the cell. The microstructural analysis confirmed the results of electrochemical evaluation. The CGO backbone seems to be too coarse, and the LSC infiltrate not sufficiently well-dispersed to create the desired large active surface area.

The cell with optimized Ni:YSZ fuel electrode showed a superior initial performance and a small degradation rate, which can be related to a better fuel electrode microstructure. However, as the oxygen electrode (LSC-CGO) only contributed to a small extent to the overall cell resistance, the overpotential related to the fuel electrode was relatively large, which led to a predominant degradation of the fuel electrode. More specifically, Ni migration and loss of percolation led to an increase of both  $R_s$  and  $R_p$  under potentiostatic conditions. Furthermore, larger leak was observed in this cell and cracks in the electrolyte have probably also contributed to the increase of  $R_s$  over time. However, these degradation phenomena were still not detrimental as compared to the overall degradation of the SoA Cell-A.

## Appendix-A

Bode plots for the tested cells under fingerprint, before and after long-term testing were analyzed. This helped in the identification of individual electrode processes. Furthermore, the extent of leak current was visualized in this manner. The plotted values are the difference between the 50% steam and 20% steam conditions, with air and oxygen. To help understand the figures better, the following points can serve as a guide:

- (i) Fuel-1: difference between 50% steam and 20% steam conditions, with oxygen on oxygen electrode
- (ii) Fuel-2: difference between 50% steam and 20% steam conditions, with air on oxygen electrode

- (iii) Fuel-avg: average of Fuel-1 and Fuel-2
- (iv) Oxygen-1: difference between 20% steam conditions on fuel electrode, under oxygen and air
- (v) Oxygen-2: difference between 50% steam conditions on fuel electrode, under oxygen and air
- (vi) Oxygen-avg: average of Oxygen-1 and Oxygen-2

In theory, the Fuel average should lie on top of/close to Fuel-1 and Fuel-2, and Oxygen average should lie close to Oxygen-1 and Oxygen-2. The distance between the average curve and the other two curves indicates the magnitude of leaks present in the cell test.

For Cell-A, in Figure 16 the magnitude of leak before the long-term test is low. After the long-term test, a significant deviation in the fuel electrode representation was found, which indicates that the leaks have increased, leading to a change in gas conversion and hence the interpretation of fuel electrode response is uncertain. The influence of the leaks on the oxygen electrode also increases after long-term testing, however, the individual and the average trends are similar. It clearly indicates the high degradation phenomenon experienced by the oxygen electrode. This confirms the observation from the DRT plots shown in Figure 7.

For Cell-B, leak present initially was higher than Cell-A as seen from Figure 17. However, the fuel and oxygen electrode responses can be easily distinguished. After the long-term test, there was a clear increase in the resistance for both oxygen

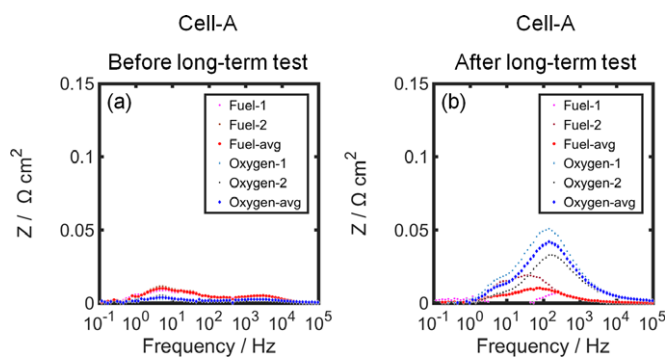


Fig. 16 Bode plots for Cell-A, (a) before, and (b) after long-term testing serving as a guide for electrode identification and the magnitude of leaks present.

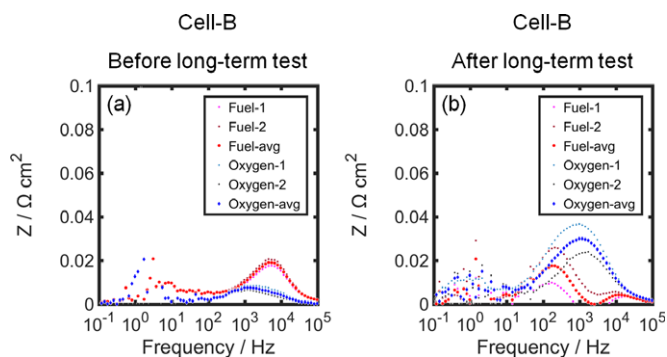


Fig. 17 Bode plots for Cell-B, (a) before, and (b) after long-term testing serving as a guide for electrode identification and the magnitude of leaks present.

and fuel electrode processes. Moreover, a shift in the summit frequency for the fuel electrode process was observed and this results in two different processes, one at a frequency of approximately 200 Hz relating to the increase in fuel electrode resistance [32], while the other at a frequency of 10 kHz remains unchanged in magnitude. The oxygen electrode response was observed at the same summit frequency while the magnitude increased, indicating towards a loss of active surface area [32]. The leak rate also increases since the difference between the two plots and the average has increased.

For the case of Cell-C, as seen from Figure 18, the magnitude of leak present before the long-term was significantly higher than the other two cells. However, fuel and oxygen electrode processes are distinguished easily. There was not a significant increase in leaks and the average response for fuel and oxygen remains equidistant from the plots. A significant shift in summit frequency was observed for the fuel electrode indicating to an increase in resistance. Oxygen electrode frequency remained similar and the magnitude of the resistance also remained unchanged.

## Appendix-B

The raw counts for the line scans during EDS analysis are displayed in Figure 19. “Inner” denotes the layer next to the electrolyte, right in the active fuel electrode. “Outer” denotes the layer in the active fuel electrode close to the support. “Support” denotes the line scan taken in the fuel electrode support.

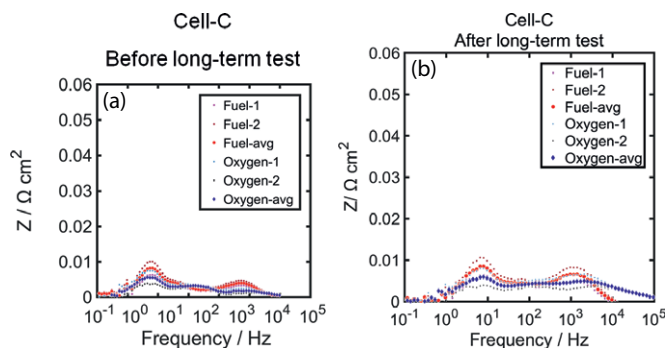


Fig. 18 Bode plots for Cell-C, (a) before, and (b) after long-term testing serving as a guide for electrode identification and the magnitude of leaks present.

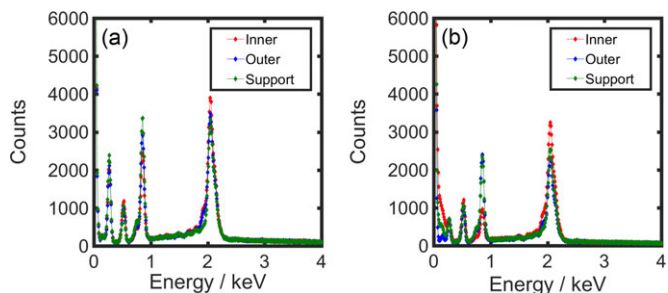


Fig. 19 Raw counts from EDS analysis of (a) Reference cell-only initial fingerprint, and (b) Long-term tested cell (Cell-C).

This was only performed for the Cell-C, and the reference cell, which is a sister cell to Cell-C and on which only initial characterization was done. The peak at 0.9 keV denotes the Ni content while for Y and Zr, the peaks are at 1.09 and 2.04 keV, respectively. Y and Zr peaks occur together. However, for the support the content differs and is clearly seen as a bend in the peak.

From the comparison, the inner Ni content seems to deplete in relative counts to that of the reference cell. This shows the depletion of Ni in the layer next to the electrolyte, which is indicated as Ni migration. These counts are used to plot the graphs in Figure 15, by taking a ratio between Ni and (Ni+YSZ) counts.

## Acknowledgements

The authors wish to thank Mr. H. Henriksen, Mrs. M. Davodi, Dr. K. Thyden and Dr. S. Koch for technical help. The authors would also like to thank Dr. A. Hauch for her scientific insight, which helped enriching this work. The research leading to these results has received funding from the European Union's Horizon 2020 framework program (H2020) for the Fuel Cells and Hydrogen Joint Technology Initiative under grant agreement no. 699892 ("Efficient Co-Electrolyser for Efficient Renewable Energy Storage-ECO").

## References

- [1] R. Lund, B. V. Mathiesen, *Applied Energy* **2015**, *142*, 389.
- [2] J. Sanz-Bermejo, J. Muñoz-Antón, J. Gonzalez-Aguilar, M. Romero, *Int. J. Hydrogen Energy* **2015**, *40*, 8291.
- [3] E. Giglio, A. Lanzini, M. Santarelli, P. Leone, *J. Energy Storage* **2015**, *1*, 2237.
- [4] S. D. Ebbesen, S. H. Jensen, A. Hauch, M. B. Mogensen, *Chem. Rev.* **2014**, *114*, 10697.
- [5] J. Aicart, F. Usseglio-Viretta, J. Laurencin, M. Petitjean, G. Delette, L. Dessemond, *Int. J. Hydrogen Energy* **2016**, *41*, 17233.
- [6] S. Mesfun, D. L. Sanchez, S. Leduc, E. Wetterlund, J. Lundgren, M. Biberacher, F. Kraxner, *Renew. Energy* **2017**, *107*, 361.
- [7] X. Sun, M. Chen, Y.-L. Liu, P. Hjalmarsson, S. D. Ebbesen, S. H. Jensen, M. B. Mogensen, P. V. Hendriksen, *J. Electrochem. Soc.* **2013**, *160*, F1074.
- [8] S. H. Jensen, C. Graves, M. Mogensen, C. Wendel, R. Braun, G. Hughes, Z. Gao, S. A. Barnett, *Energy Environ. Sci.* **2015**, *8*, 2471.
- [9] P. Hjalmarsson, X. Sun, Y. L. Liu, M. Chen, *J. Power Sources* **2014**, *262*, 316.
- [10] A. Hauch, K. Brodersen, M. Chen, M. B. Mogensen, *Solid State Ionics* **2016**, *293*, 27.
- [11] X. Zhang, J. E. O'Brien, R. C. O'Brien, G. K. Housley, *J. Power Sources* **2013**, *242*, 566.
- [12] T. Kushi, *Int. J. Hydrogen Energy* **2017**, *42*, 9396.
- [13] R. Knibbe, M. L. Traulsen, A. Hauch, S. D. Ebbesen, M. Mogensen, *J. Electrochem. Soc.* **2010**, *157*, B1209.
- [14] A. Hauch, S. D. Ebbesen, S. H. Jensen, M. Mogensen, *J. Electrochem. Soc.* **2008**, *155*, 1184.
- [15] M. Chen, Y.-L. Liu, J. J. Bentzen, W. Zhang, X. Sun, A. Hauch, Y. Tao, J. R. Bowen, P. V. Hendriksen, *J. Electrochem. Soc.* **2013**, *160*, F883.
- [16] F. Tietz, D. Sebold, A. Brisse, J. Schefold, *J. Power Sources* **2013**, *223*, 129.
- [17] P. Hjalmarsson, X. Sun, Y. L. Liu, M. Chen, *J. Power Sources* **2013**, *223*, 349.
- [18] S. B. Adler, *Chem. Rev.* **2004**, *104*, 4791.
- [19] P. Moçoteguy, A. Brisse, *Int. J. Hydrogen Energy* **2013**, *38*, 15887.
- [20] D. Ding, X. Li, S. Y. Lai, K. Gerdes, M. Liu, *Energy Environ. Sci.* **2014**, *7*, 552.
- [21] K. K. Hansen, V. Gil, *ECS Trans.* **2014**, *64*, 41.
- [22] S. D. Ebbesen, C. Graves, A. Hauch, S. H. Jensen, M. Mogensen, *J. Electrochem. Soc.* **2010**, *157*, B1419.
- [23] S. H. Jensen, A. Hauch, P. V. Hendriksen, M. Mogensen, *J. Electrochem. Soc.* **2009**, *156*, B757.
- [24] M. Chen, X. Sun, C. Chatzichristodoulou, S. Koch, P. V. Hendriksen, M. B. Mogensen, *ECS Trans.* **2017**, *78*, 3077.
- [25] C. Graves, *Ravdav* **2012**.
- [26] K. Thydén, Y. L. Liu, J. B. Bilde-Sørensen, *Solid State Ionics* **2008**, *178*, 1984.
- [27] J. I. Gazzarri, O. Kesler, *J. Power Sources* **2008**, *176*, 155.
- [28] R. R. Mosbæk, J. Hjelm, R. Barfod, J. Høgh, P. V. Hendriksen, *Fuel Cells* **2013**, *13*, 605.
- [29] S. H. Jensen, J. Hjelm, A. Hagen, M. Mogensen, in *Handbook of Fuel Cells – Fundamentals, Technology and Applications*, Vol. 6 (Eds. W. Vielstich, H. Yokokawa, H. A. Gasteiger), John Wiley & Sons, Ltd., Chichester, United Kingdom, **2009**, pp. 792.
- [30] M. Rao, X. Sun, A. Hagen, *J. Electrochem. Soc.* **2018**, *65*, 748.
- [31] M. B. Mogensen, A. Hauch, X. Sun, M. Chen, Y. Tao, S. D. Ebbesen, K. V. Hansen, P. V. Hendriksen, *Fuel Cells* **2017**, *17*, 434.
- [32] S. H. Jensen, A. Hauch, P. V. Hendriksen, M. Mogensen, N. Bonanos, T. Jacobsen, *J. Electrochem. Soc.* **2007**, *154*, B1325.